

www.acsanm.org Article

Coupling Light in Ion-Exchanged Waveguides by Silver Nanoparticle-Based Nanogratings: Manipulating the Refractive Index of Waveguides

Maedeh Aslani, Razieh Talebi,* and Daryoosh Vashaee



Cite This: ACS Appl. Nano Mater. 2022, 5, 5439–5447



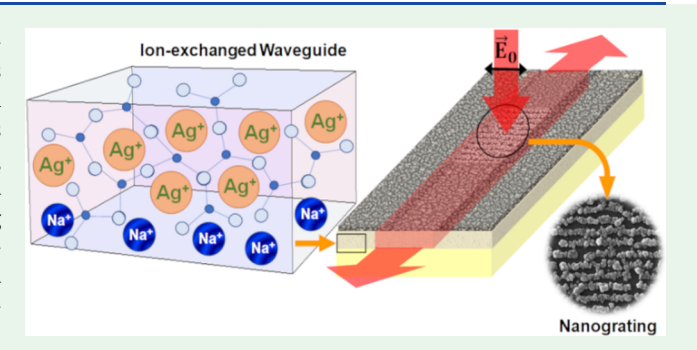
ACCESS I

Metrics & More

Article Recommendations

Supporting Information

ABSTRACT: We report the fabrication and properties of ion-exchanged optical waveguides based on low-cost soda-lime glasses embedded with silver ions and nanoparticles. Using the thermal ion-exchange process, we embed silver ions into soda-lime glasses by covering the glasses with different ratios of AgNO₃:NaNO₃ molten salt (2:98, 4:96, and 6:94) at 350 °C. The ion-exchanged glasses containing silver nanoparticles were characterized by using X-ray fluorescence spectroscopy, UV—visible spectroscopy, the X-ray diffraction technique, X-ray photoelectron spectroscopy, and atomic force microscopy of the surface. It is shown that the ion-exchanged glasses make low-loss optical waveguides. Furthermore, we evaluate the refractive index of ion-exchanged waveguides by



laser coupling into the waveguide. For this purpose, the ion-exchanged glasses were coated with a silver chloride thin film loaded with silver nanoparticles (Ag-AgCl). When the Ag-AgCl layer is irradiated by a polarized coherent light beam, silver nanograting is formed on the surface of the ion-exchanged glass, and the light beam is simultaneously coupled into the glass. The line-space of nanograting determines the effective refractive index of the ion-exchanged glass. Although we expected the sample with the highest ratio of AgNO₃:NaNO₃ salt (6:94) to have the largest refractive index, our results demonstrate that the ion-exchanged sample with 4% AgNO₃ has the largest effective refractive index, which is due to the penetration of more silver ions and nanoparticles in the glass matrix. Therefore, it is further demonstrated that using a Ag-AgCl layer on an ion-exchanged waveguide is an effective method for coupling light into the waveguides and measuring its refractive index. The mentioned coupling technique in combination with easily fabricated ion-exchanged waveguide has served as an excellent platform for applications in integrated optical circuits.

KEYWORDS: ion-exchanged glass, silver nanoclusters, Ag-AgCl thin film, silver nanograting, surface plasmon resonance

INTRODUCTION

Over the last few decades, many studies in doping metal nanoparticles into a glass substrate investigated the thermal ion-exchange (IE) process. ¹⁻⁴ In this process, the glasses are covered by molten salt, including metal ions, which replace alkali ions in the glass matrix during a thermal process. ¹⁻⁴ Penetration of metal ions such as silver ions (Ag⁺s) into a glass induces positive stress due to the different ionic radius and polarizability from those of sodium ions (Na⁺s), accompanied by modification of its refractive index. ⁴⁻⁷ Changing the molten salt composition makes it possible to manipulate the refractive index of the glass induced by the IE process. ⁶

The IE process increases the refractive index of the glass due to the formation of silver clusters in the glass matrix. The high refractive index glasses are excellent candidates for designing solid-state lasers and creating broadband optical waveguides, which are utilized in integrated optical circuits. Ion-exchanged waveguides are also used to couple light into the photonic structure, such as plasmons in array gratings and slab. Is,16 Furthermore, ion-exchanged waveguides

are intended for classical/quantum optical communications and sensing. 17,18

The refractive index of Ag⁺/Na⁺ ion-exchanged glasses depends on the concentration of Ag⁺s introduced into the glass matrix. Ag⁺s, driven into the glass matrix from molten salt by a thermal process, penetrate a few micrometers into the glass matrix, but they are not often uniformly distributed through the glass. Therefore, the concentration of silver in the glass matrix can be represented by a gradient profile, which rapidly decreases inward. Similarly, the refractive index of an ion-exchanged glass presents a gradient-index distribution. Silver

Received: January 28, 2022 Accepted: March 31, 2022 Published: April 8, 2022





Therefore, an effective refractive index for the ion-exchanged glass should be considered and measured. 4,6

One of the significant challenges of using ion-exchanged glasses as a waveguide is coupling the light beam into the waveguides. Among different coupling mechanisms, the prism coupling approach and periodic nanostructures are the most appropriate methods for coupling the light beam into ion-exchanged glasses. In the prism coupling technique, a high-index prism guides incident light into the waveguide. For this purpose, phase matching must occur between the incident wave and guided mode. In addition, fabricating periodic nanostructures at the surface of a waveguide is also an effective method for light coupling. 23,24

In this paper, we supply an original and novel way to couple light into the ion-exchanged waveguides, which is based on a silver chloride thin film loaded with silver nanoparticles (AgAgCl). Nanograting is formed in the Ag-AgCl thin film by irradiating a linearly polarized laser beam to the film. The nanograting is an aperture for coupling the light beam into the ion-exchanged waveguides. Furthermore, the line-space of the nanograting indicates the effective refractive index of the substrate. ^{9,23–25}

Ion-exchanged glasses with three different silver concentrations are prepared in this research. The atomic compositions of these glasses are studied using X-ray fluorescence (XRF) spectroscopy. X-ray photoelectron spectroscopy (XPS) is also used to evaluate the surface chemical compositions of ion-exchanged glasses. Finally, the crystallinity of the prepared sample is examined by the X-ray diffraction (XRD) technique.

The optical properties of ion-exchanged glasses are characterized by UV-visible spectrometry. Afterward, the ion-exchanged glasses are covered by the Ag-AgCl thin film and irradiated by a low-power laser to couple the beam into the glass. Simultaneously, nanograting is formed in the Ag-AgCl thin film. Ultimately, the effective refractive indices of ion-exchanged glasses are determined by measuring the line-spacing of the nanogratings using scanning electron microscopy (SEM) images and their fast Fourier transform (FFT) features.

EXPERIMENTAL SECTION

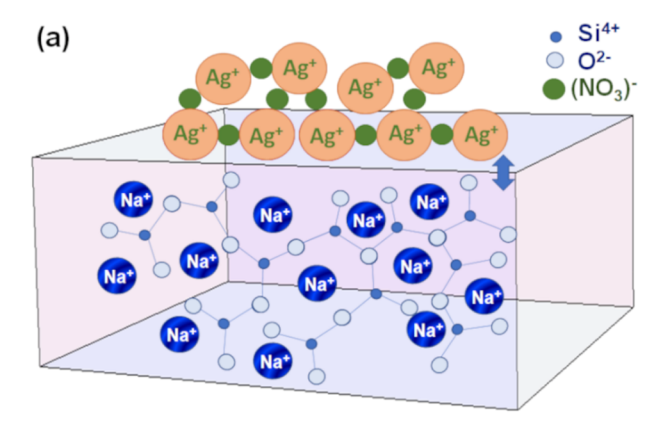
This section focuses on the preparation and characterization of ion-exchanged glasses. Afterward, the deposition technique for coating ion-exchanged glasses by the Ag-AgCl thin film will be described. Finally, the irradiation process of ion-exchanged glasses coated by the Ag-AgCl thin film is explained.

Preparation of lon-Exchanged Glasses. Commercial soda-lime glasses with a thickness of 1 mm were used for the IE process. The chemical components of the soda-lime glass (% w/w) are 66.16 SiO₂, 20.90 Na₂O, 5.85 CaO, 4.46 MgO, 1.16 Al₂O₃, 0.88 K₂O, 0.29 SO₃, 0.12 As₂O₃, and 0.03 Fe₂O₃, which are measured by an S4 Pioneer XRF.

In the IE process, Ag^+s in silver nitrate $(AgNO_3)$ salt, mixed with sodium nitrate $(NaNO_3)$ salt, replaced Na^+s in soda-lime glass by a thermal process. We carried out the IE process at 350 °C for 30 min. In Figure 1a and Figure 1b, the IE process in the glass matrix is schematically shown at the beginning and the end of the annealing process, respectively. The maximum depth that Ag^+s penetrate in the glass matrix depends on the duration of thermal treatment. 26

Three samples with different ratios of AgNO₃ to NaNO₃ described as follows were prepared:

- 1) 2% AgNO₃:98% NaNO₃ (IE 2%)
- 2) 4% AgNO₃:96% NaNO₃ (IE 4%)
- 3) 6% AgNO₃:94% NaNO₃ (IE 6%)



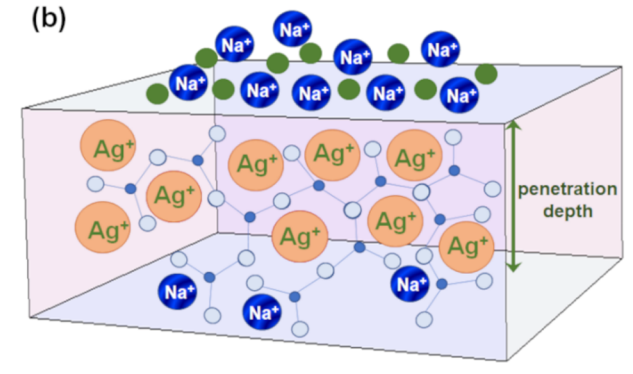


Figure 1. Scheme of the IE process (a) at the beginning and (b) at the end of thermal treatment.

After the IE process, all samples were soaked in diluted hydrochloric acid to remove the remaining salts on the surface. In the last stage, the samples were rinsed with distilled water. As a result, the ion-exchanged samples were faint yellow after the IE process, ²² as represented in Figure S1 of the Supporting Information.

In Table 1, the chemical compositions of IE 2%, IE 4%, and IE 6% samples are listed. Although the absolute values of the XRF readings

Table 1. XRF Analysis of Ion-Exchanged Samples (% w/w)

component	IE 2%	IE 4%	IE 6%
SiO_2	68.58	72.73	78.80
Na_2O	19.00	13.80	7.08
CaO	5.81	6.05	5.52
MgO	4.04	4.35	4.86
Al_2O_3	1.11	1.14	1.25
K_2O	0.75	0.88	1.02
Ag	0.11	0.33	0.57
SO_3	0.30	0.37	0.46
As_2O_3	0.12	0.15	0.20
Fe ₂ O ₃	0.03	0.03	0.03

may not be accurate, they give us appreciable information about the glass compositions before and after the IE process.

As shown in Table 1, the primary component of ion-exchanged samples is silicon dioxide (SiO₂). The silver (Ag) content appears in all ion-exchanged samples, although its amount is less than 1%. Comparing the sodium oxide (Na₂O) content of soda-lime glass with that in ion-exchanged samples, the Na₂O content in ion-exchanged samples is decreased. Therefore, Na⁺s were replaced by Ag⁺s in the IE process. ²⁷ In the glass, the presence of impurities, such as arsenic trioxide (As₂O₃) and ferric oxide (Fe₂O₃), promotes the reduction of Ag⁺s into metallic clusters. ^{22,28}

Characterization of lon-Exchanged Samples. The optical properties of ion-exchanged samples were measured by UV-visible

spectrometry, which can provide information about the energy gap and band structure of the glasses.²⁹ For this purpose, a UV—vis—NIR JASCO V-670 spectrophotometer was used to measure the optical density and diffuse reflectance spectra of the ion-exchanged samples. Optical density (OD), which is a criterion of absorption, is defined as

optical density =
$$-\log(T/T_0)$$
 (1)

where T and T_0 are the intensities of the transmitted light passing through the ion-exchanged samples and the soda-lime glasses, respectively.²⁵

Figure 2a shows the optical density spectra of IE 2%, IE 4%, and IE 6% samples. In Figure 2a, each spectrum includes an intense peak

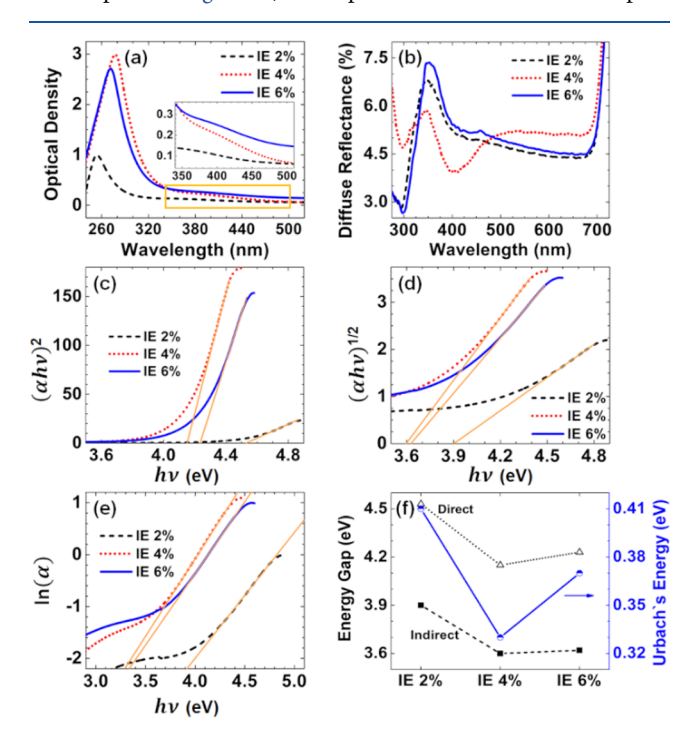


Figure 2. (a) Optical density spectra, (b) diffuse reflectance spectra, (c) Tauc plots for determining direct energy gaps, (d) Tauc plots for determining indirect energy gaps, (e) $\ln(\alpha)$ versus $h\nu$ plot used to calculate Urbach's energy, and (f) comparing the direct and indirect energy gaps and Urbach's energy of IE 2%, IE 4%, and IE 6% samples.

below 300 nm and a small broad hump in the vicinity of 400 nm, respectively, ascribed to the absorption band of Ag^+s and surface plasmon resonance (SPR) of silver nanoclusters. The SPR hump is better shown in the inset of Figure 2a.

To distinguish the extinction peak of Ag^+s from the SPR hump of silver nanoclusters in the optical density spectrum, we fitted two Lorentz curves to each spectrum, as shown in Figure S2 of the Supporting Information. The peak position (λ) and the full width at half-maximum $(\Delta\lambda)$ of the fitted Lorentz curves are also reported in Table S1 of the Supporting Information.

In the IE process at 350 °C (below 400 °C), silver atoms are mainly in the form of Ag⁺s.¹⁹ Some Ag⁺s in the glass matrix are neutralized by continuing the annealing process, and silver nanoclusters are formed.²² Although no significant SPR absorption peak of silver nanoclusters was seen,³⁰ Table S1 shows that a small number of Ag⁺s are neutralized and form silver nanoclusters. By using the data in Table S1, the average size of silver nanoclusters, which are embedded in the glass matrix, can be calculated as the following relation³⁰

$$D = \frac{V_{\rm f} \lambda_{\rm SPR}^2}{\pi c \Delta \lambda_{\rm SPR}} \tag{2}$$

where D is the average diameter of silver nanoclusters, $V_f = 1.39 \times 10^6$ m/s is the Fermi velocity of the electrons in the bulk silver, c is the

speed of light in vacuum, $\lambda_{\rm SPR}$ is the characteristic wavelength of silver nanoclusters, and $\Delta\lambda_{\rm SPR}$ is the full width at half-maximum. The average sizes of silver nanoclusters in IE 2%, IE 4%, and IE 6% samples are approximately 0.9, 3.2, and 3.1 nm, respectively. Therefore, the clusters in IE 2%, IE 4%, and IE 6% samples, respectively, contain about 16, 819, and 736 atoms. The silver nanoclusters are larger in the IE 4% sample, consisting of more atoms than the other samples.

Figure 2b shows the diffuse reflectance spectra of IE 2%, IE 4%, and IE 6% samples. Since silver nanoparticles of ion-exchanged samples can scatter light, diffuse reflectance spectroscopy (DRS) is preferred to direct reflectance spectroscopy for ion-exchanged samples. In Figure 2b, the dips around 400 nm, approximately near the SPR peak, can be discerned, which is more apparent for the IE 4% sample. The reflectance spectrum of the IE 4% sample rises rapidly at 400 nm such that, above 480 nm, its reflectance is higher than the other samples.

Diffuse reflectance spectra can be used to estimate the energy gaps of the samples, which contain nanoparticles, using the Kubelka–Munk equation. The absorption spectroscopy of an ion-exchanged glass is also helpful to determine the energy gap by Tauc's law, defined as 9,32

$$\alpha h v = B(h v - E_g)^n \tag{3}$$

where α is the absorption coefficient, hv is the photon energy, B is the band tailing parameter, and $E_{\rm g}$ is the energy gap. The absorption coefficient is proportional to optical density according to αd = 2.303(OD), where d is the thickness of the sample.^{9,32} In relation 3, n= 1/2 and 2, respectively, correspond to the allowed direct and indirect energy gaps.³² The energy gaps of ion-exchanged samples are obtained from the intercepts of the extrapolated linear fit to relation 3, which are shown by the orange lines in Figure 2c,d. The direct energy gaps of IE 2%, IE 4%, and IE 6% samples are 4.53, 4.15, and 4.23 eV, respectively. The indirect energy gaps of IE 2%, IE 4%, and IE 6% samples are 3.90, 3.60, and 3.62 eV, respectively. Interestingly, the lowest energy gaps are recorded for the IE 4% sample, which has larger silver nanoclusters. Therefore, for having a smaller bandgap in ion-exchanged glasses and better growth and diffusion of silver nanoparticles in the glass matrix, 4% of AgNO3 in molten salt is enough.

Ion-exchanged glasses are known as amorphous semiconducting materials. In such materials, an absorption edge, called Urbach's edge, arises from structural disorientations and randomness. ³² For evaluating the degree of structural disorder in ion-exchanged samples, Urbach's energy is calculated by the following relation ³²

$$\alpha = \alpha_0 \exp(hv/E_v) \tag{4}$$

where α_0 is a constant and $E_{\rm u}$ is Urbach's energy. Therefore, the absorption spectrum is used to obtain Urbach's energy. ³³ In Figure 2e, $\ln(\alpha)$ versus hv is plotted for IE 2%, IE 4%, and IE 6% samples. According to relation 4, the reciprocal of the line slopes, fitted to the plots in Figure 2e, determines Urbach's energy. For IE 2%, IE 4%, and IE 6% samples, Urbach's energies are 0.41, 0.33, and 0.37 eV, respectively. Therefore, the IE 2% sample has a poor crystalline structure.

The energy gaps and Urbach's energy of IE 2%, IE 4%, and IE 6% samples are compared in Figure 2f. Unexpectedly, both direct and indirect energy gaps and also Urbach's energy in the IE 4% sample are lower than those in the IE 6% sample. The decrease in the energy gaps of the IE 4% sample is attributed to the increase in the size of the silver nanoclusters and the decrease in structural disorder, in agreement with the smaller Urbach's energy.³⁴

The crystallinity of ion-exchanged samples was also examined by XRD analysis, as shown in Figure S3. The XRD profiles of IE 2% and IE 4% samples do not illustrate any significant peak. The XRD pattern of the IE 6% sample shows two sharp peaks at $2\theta=29.41$ and 31.73° , corresponding to (110) and (111) of silver oxide (Ag₂O), respectively. Therefore, the increase in the absorption spectrum of the IE 6% sample, from 400 nm to higher wavelengths, is due to the Ag₂O crystals on the surface of this sample. Despite the two peaks in

the XRD pattern of the IE 6% sample, the nature of ion-exchanged glasses is still amorphous. $^{37,38}\,$

The surface chemical compositions of the ion-exchanged glasses were recorded by XPS. The XPS measurements were performed using an XPS/UVS-SPECS system equipped with a PHOIBOS 150 analyzer (<1 eV resolution). The XPS broad spectra of soda-lime glass and IE 2%, IE 4%, and IE 6% samples are presented in Figure S4 in the Supporting Information. In the mentioned spectra, the peaks attributed to Si 2p, Si 2s, C 1s, Ag 3d, O 1s, and Na 1s are clarified.

The high-resolution Ag 3d core-level spectra of IE 2%, IE 4%, and IE 6% samples are displayed in Figure 3a and are compared with the

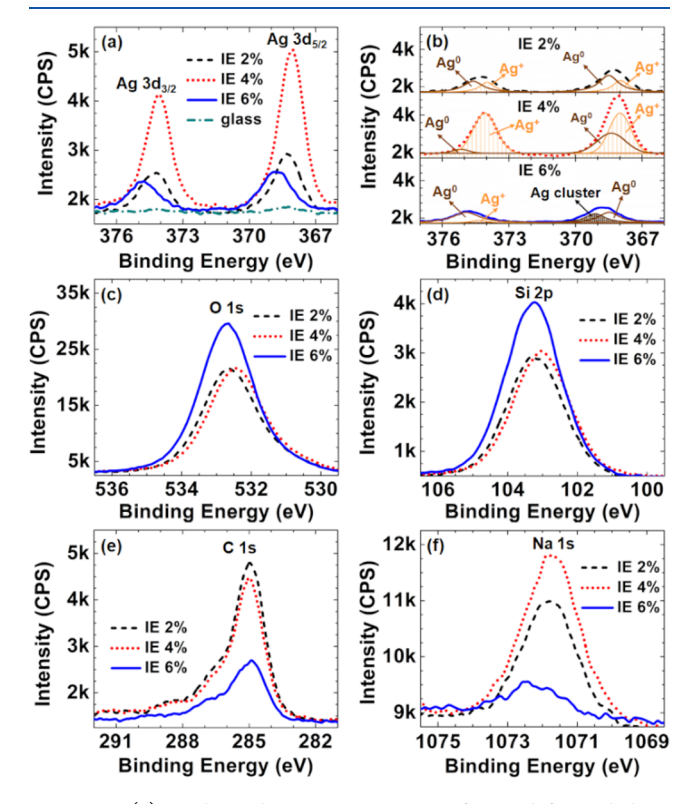


Figure 3. (a) High-resolution XPS spectra of Ag 3d for soda-lime glass and IE 2%, IE 4%, and IE 6% samples. (b) Ag 3d core-level spectra, (c) O 1s core-level spectra, (d) Si 2p core-level spectra, (e) C 1s core-level spectra, and (f) Na 1s core-level spectra of IE 2%, IE 4%, and IE 6% samples.

XPS spectrum of soda-lime glass. The Ag 3d core-level spectrum consists of Ag $3d_{3/2}$ and Ag $3d_{5/2}$ peaks. The two peaks are separated by approximately 6 eV. The Ag 3d peaks of the IE 4% sample indicate higher intensity.

In Figure 3a, the Ag 3d core-level spectrum of the IE 6% sample unexpectedly shows the lowest peak compared to other samples. The optical density spectra in Figure 2a and reflectance spectra in Figure 2b clearly show that the population of silver clusters in the IE 6% sample is much larger than that in the IE 2% sample.

The strange behavior of the XPS spectrum of Ag 3d for the IE 6% sample can be attributed to a large population of silver clusters and Ag₂O crystals on the surface of this sample. The surface fullness of the IE 6% sample blocks the low-energy electrons emitted from the silver atoms from reaching the XPS detector. The blue shift of Ag 3d peaks for the IE 6% sample also confirms that only the high-energy electrons pass through the surface of this sample and reach the detector.

XPS data is analyzed to identify the chemical states of silver particles (Ag⁺ or Ag⁰) located on the surface of ion-exchanged samples. ²⁵ In Figure 3b, Ag 3d peaks are deconvoluted into four fitted peaks for the IE 2%, IE 4%, and IE 6% samples. In Table S2, the intensity, full width at half-maximum (FWHM), and binding energy

of Ag^0 and Ag^+ , corresponding to each fitted peak in Figure 3b, are reported.

For the IE 2% sample, the population of Ag^0s and Ag^+s on the sample surface is almost the same, while for the IE 4% sample, silver is mostly Ag^+s . The $Ag~3d_{3/2}$ and $Ag~3d_{5/2}$ peaks of IE 6% samples are shifted toward higher energy, evidencing that Ag^+s on the surface are neutralized in the air, forming silver clusters $(Ag^0)_n$. 22,39 Furthermore, some silver nanoclusters on the surface of IE 6% are capped with $Ag_2O.^{36}$

In Figure 3c, the O 1s core levels of IE 2%, IE 4%, and IE 6% samples are shown. The O 1s peak of the IE 6% sample is more intense than the other samples. As mentioned before, silver nanoclusters on the IE 6% sample surface are oxidized, forming a Ag₂O shell around the silver nanoparticles.³⁶

In Figure 3c, the O 1s peak of the IE 4% sample is shifted toward lower energy compared to other samples. The non-bridging oxygens (NBO) have lower energy than bridging oxygens (BO). The XPS peak of NBO is seen at 530 nm while that of BO is observed at 533 nm. 40 The deconvolutions of the O 1s core-level spectra for soda-lime glass and the IE 2%, IE 4%, and IE 6% samples are shown in Figure S5 of the Supporting Information.

In Figure 3d, Si 2p core levels of IE 2%, IE 4%, and IE 6% samples are demonstrated. The height of the Si 2p peak for the IE 6% sample is substantially larger than the other samples due to the presence of the Si–O–Si bond on the sample surface. Ag⁺s tend to neutralize and form silver clusters on the surface during the IE process. Therefore, the number of Si–O–Ag⁺ linkages near the surface decreases compared to Si–O–Si linkages. For the IE 4% sample, the Si 2p peak is shifted toward lower energy. This shift is related to the formation of more Si–C-, Si–OH-, and SiO₂-like bands. 30

Figure 3e demonstrates the C 1s core levels of IE 2%, IE 4%, and IE 6% samples, which appear on the surface of the ion-exchanged samples due to surface contamination. Increasing the AgNO₃ ratio in the IE process, the surface contamination decreases. The C 1s corelevel spectra of the ion-exchanged samples are compared with a clean soda-lime glass, as shown in Figure S6 of the Supporting Information. The high peak of C 1s of soda-lime glass before the IE process shows that the IE process decreases the surface contamination.

Figure 3f compares the Na 1s peaks of IE 2%, IE 4%, and IE 6% samples. Almost all Na⁺s are replaced by Ag⁺s in the IE 6% sample during the IE process. Therefore, the population of Na⁺s is too low on the surface of the IE 6% sample, which leads to the lower intensity of the Na 1s core-level spectrum. In contrast, for the IE 4% sample, it seems that a large number of Na⁺s are not replaced. As mentioned earlier, the surface of the IE 4% sample, compared to the IE 6% sample, is not densely covered by Ag⁺s; as such, a considerable redistribution likely occurs in the IE 4% sample, i.e., Ag⁺s diffuse inside the glass matrix and Na⁺s inside the glass matrix diffuse toward the surface. ⁴¹ Furthermore, more Ag⁺s from AgNO₃ salt have the chance to replace Na⁺s in the IE 4% sample during the IE process.

The surface morphology is investigated by atomic force microscopy (AFM) to observe the distribution of the silver nanoparticles on the surface of the ion-exchanged samples. The AFM images of the surface of IE 2%, IE 4%, and IE 6% samples are shown in Figure 4a—c, respectively.

Figure 4a demonstrates that the surface of the IE 2% sample is sparse, and the average separation of the silver nanoparticles in this sample is significantly larger than in other samples. The population of silver nanoclusters on the surface of the IE 4% sample is more than the IE 2% sample, as shown in Figure 4b. Figure 4c demonstrates that silver nanoclusters densely cover the surface of the IE 6% sample. Although the size of silver nanoclusters on the surface of the IE 4% sample is larger than that on the IE 6% sample, the average separation of the silver nanoclusters on the IE 6% sample is less than that on the IE 4% sample. AFM analysis of the surface morphology and roughness of ion-exchanged samples is shown with more detail in Figure S7 in the Supporting Information.

Ag-AgCl Thin Film on lon-Exchanged Glasses. A Ag-AgCl thin film was deposited at room temperature on the surface of ion-exchanged glasses, at 5×10^{-5} mbar pressure, in two subsequent

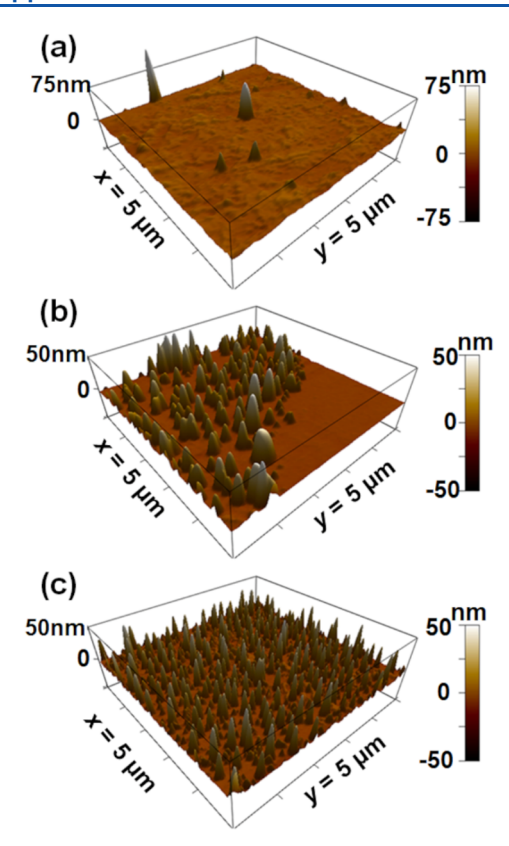


Figure 4. AFM images of (a) IE 2%, (b) IE 4%, and (c) IE 6% samples.

procedures by the thermal evaporation technique. First, to excite the lowest order transverse electric mode (TE $_0$), at the visible-light region, the AgCl layer with a thickness of 50 \pm 2 nm was evaporated to form a waveguide on the surface of the ion-exchanged samples. Afterward, a 10 \pm 2 nm-thick silver was coated on the AgCl layer. The thickness of the silver layer is too small to form a continuous layer at room temperature with this approach. Instead, silver nanoparticles form on the surface of the AgCl film. In Figure 5a and Figure 5b, the ion-exchanged glasses, with and without the Ag-AgCl layer on the surface, are shown, respectively.

lirradiating the Samples. The ion-exchanged samples with a few micrometers' penetration depth, covered by a 60 nm-thick Ag-AgCl layer, were irradiated with the linearly polarized continuous-wave laser beams. A He—Ne laser beam with a wavelength of 632.8 nm and power of 4 mW and the second harmonic generation of the Nd:YAG laser beam at a wavelength of 532 nm and power of 44 mW were used to irradiate the samples. The two different laser beams were used to study the dependence of the refractive index of the ion-exchanged samples on the wavelength. Since the output power of lasers is not the same, the different exposure times are considered for sample irradiation, 55 min for the He—Ne laser and 5 min for the Nd:YAG laser. To polarize the laser beam, we used a Glan—Taylor calcite polarizer (Thorlabs code: GT10-A) with an accuracy of 5 min.

When the Ag-AgCl thin film is irradiated by the laser beam in the $(\pm z)$ direction, the silver nanoparticles scatter the incident laser beam. A part of scattered waves propagates in AgCl waveguide in $(\pm y)$ directions, which is perpendicular to both the incident direction $(\pm z)$ and polarization direction $(\pm x)$ of the beam (\vec{E}_0) , as schematically shown in Figure 5c.

The interference of the incident and propagated beams in AgCl waveguide results in bright and dark fringes in the AgCl thin film. The silver nanoparticles disappear in the bright fringes of the interference pattern. Therefore, silver nanoparticles were aligned in the dark fringes of the interference. Figure 5d schematically shows the aligned silver nanoparticles.

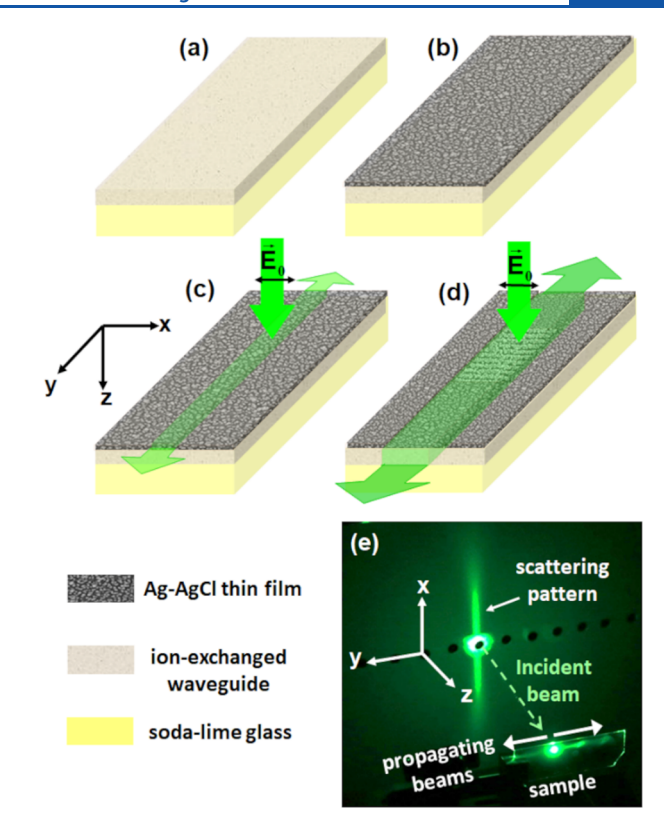


Figure 5. (a) Ion-exchanged glass in which Ag⁺s and Ag nanoparticles penetrate a few micrometers in the glass matrix; (b) Ag-AgCl layer on the surface of the ion-exchanged glass with a thickness of 60 nm; (c) the normal incident laser beam is scattered by silver nanoparticles and then propagates in the AgCl thin film; (d) the formation of silver nanograting on the surface of the sample couples the laser beam into the ion-exchanged waveguide; (e) propagating beam in the sample and the scattering pattern after the formation of the silver grating.

The periodic structure of the silver nanoparticles acts as an optical grating, which could couple the laser beam into the ion-exchanged glass. As a result, the ion-exchanged glass behaves as a slab waveguide. In Figure 5e, a screen is placed between the laser and the sample. The laser beam passes through one of the holes on the screen to reach the sample. The coupled beam, which is propagating in the ion-exchanged glass, is illustrated in Figure 5e. The direction of the propagating beams in the ion-exchanged glass $(\pm y)$ is perpendicular to the incident direction $(\pm z)$ and the direction of grating lines $(\pm x)$. As shown in Figure 5e, a scattering pattern appears in the direction of the grating lines on the screen.

■ RESULTS AND DISCUSSION

The formation of optical gratings on the surface of ion-exchanged glass not only offers an appropriate method of coupling the laser beam into the ion-exchanged waveguide, but it also offers a straightforward approach to quantify the effective refractive index of the ion-exchanged glasses.²⁴

In the normal incident case, the line-space (d) of the periodic nanostructures, formed in Ag-AgCl thin films, depends on the wavelength (λ) of the incident beam and the effective refractive index of the substrate ($n_{\rm eff}$) according to the following relation²⁴

$$d = \frac{\lambda}{n_{\text{eff}}} \tag{5}$$

The soda-lime glass and IE 2%, IE 4%, and IE 6% samples, coated by the Ag-AgCl thin film, are irradiated by the linearly

polarized He-Ne laser beam at a wavelength of 632.8 nm. The surfaces of the samples after laser irradiation are imaged using scanning electron microscopy (SEM). The fast Fourier transform (FFT) feature of each SEM image is used to determine the line-space of the periodic nanostructure.

The SEM images of the periodic structure, which are formed on the surface of soda-lime glass and the IE 2%, IE 4%, and IE 6% samples after laser irradiation, are shown in Figure 6a-d, respectively. The bright particles in the SEM images are silver nanoparticles, aligned with the laser polarization direction (E_0) .

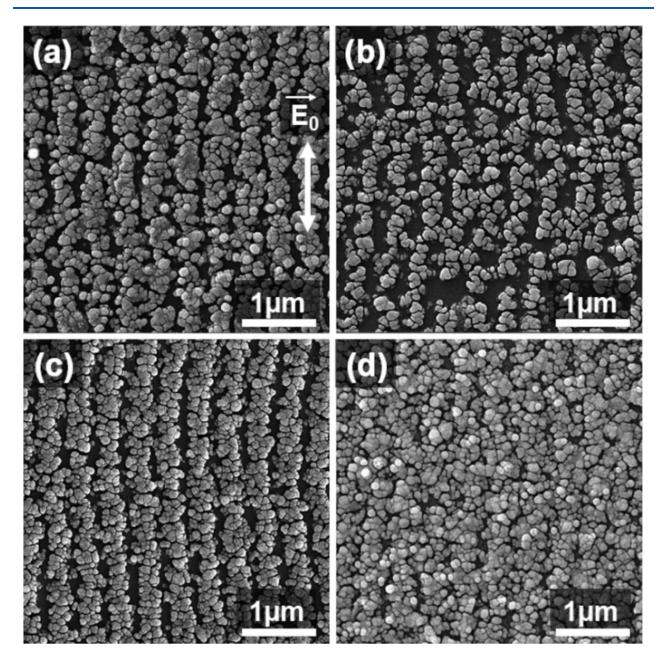


Figure 6. SEM images of the periodic nanostructures formed by irradiating laser beam with a wavelength of 632.8 nm on the surface of (a) soda-lime glass, (b) IE 2% sample, (c) IE 4% sample, and (d) IE 6% sample.

The FFT features, which are in the reciprocal space of the SEM images of Figure 6, are shown in Figure S8 of the Supporting Information. A pair of sickle-shaped lines is seen in each FFT feature, which evidences the formation of the periodic structures.

The line-spaces of periodic nanostructures in Figure 6a-d are approximately 427, 413, 400, and 411 nm, respectively. Accordingly, the effective refractive indices of the soda-lime glass and IE 2%, IE 4%, and IE 6% samples, calculated in relation 5, are reported in Table 2.

The soda-lime glass and IE 2%, IE 4%, and IE 6% samples covered by the Ag-AgCl thin film are also irradiated by the Nd:YAG laser at a wavelength of 532 nm. The effective refractive indices of these samples are also calculated by analyzing the FFT features and based on eq 5. The results are reported in Table 2.

Figure 2a and Figure 2b, respectively, showing the optical density and diffuse reflectance spectra of the IE 2%, IE 4%, and IE 6% samples, could also be used to measure the refractive index of the ion-exchanged samples. The refractive index of the ion-exchanged samples versus wavelength can be obtained using the following relation

Table 2. Effective Refractive Indices of the Soda-Lime Glass and the IE Samples, Measured at Two Wavelengths

samples	methods	@632.8 nm	@532 nm
IE 0%	FFT	1.48 ± 0.02	1.50 ± 0.02
	RID		
	Brewster	1.46 ± 0.03	1.48 ± 0.03
IE 2%	FFT	1.53 ± 0.02	1.54 ± 0.02
	RID	1.53 ± 0.01	1.55 ± 0.01
	Brewster	1.53 ± 0.03	1.56 ± 0.03
IE 4%	FFT	1.57 ± 0.03	1.60 ± 0.02
	RID	1.58 ± 0.01	1.59 ± 0.01
	Brewster	1.58 ± 0.02	1.58 ± 0.03
IE 6%	FFT	1.53 ± 0.02	1.55 ± 0.02
	RID	1.54 ± 0.01	1.56 ± 0.01
	Brewster	1.55 ± 0.03	1.56 ± 0.03

$$n = \frac{(1+R) + \sqrt{4R - (1-R)^2 k^2}}{(1-R)} \tag{6}$$

where R is the normalized reflectance and k is the extinction coefficient, which is defined as

$$k = \frac{\alpha \lambda}{4\pi} \tag{7}$$

where k and R can be obtained from Figure 2a and Figure 2b, respectively.

The refractive index dispersion (RID) curves of the IE 2%, IE 4%, and IE 6% samples are shown in Figure 7. The

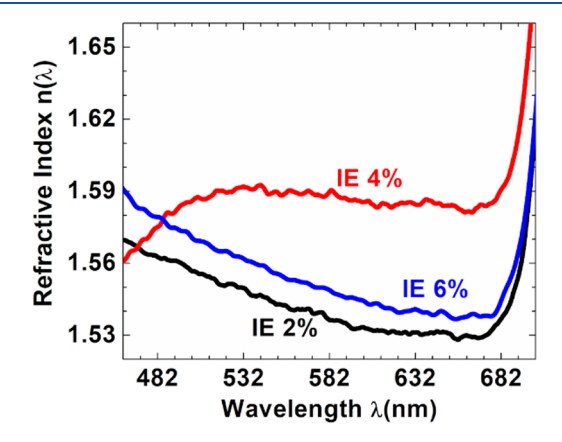


Figure 7. Refractive index versus wavelength for the IE 2%, IE 4%, and IE 6% samples.

refractive indices at wavelengths of 532 and 632.8 nm are extracted from Figure 7 and reported in Table 2. The refractive indices extracted from Figure 7 agree well with those obtained from the FFT features of the SEM images.

Furthermore, the effective refractive indices of the soda-lime glass and the ion-exchanged samples are calculated by measuring Brewster's angle at the two wavelengths of 632.8 and 532 nm. These results are reported in Table 2, matching well with those calculated by FFT analysis and the RID curves.

Table 2 shows that the effective refractive indices of the ionexchanged samples are larger than that of the soda-lime glass, which is due to the large population of the Ag+s in the glass matrix. The IE 4% sample has the largest refractive index at both wavelengths. In the IE 4% sample, more Ag+s penetrate the glass matrix than the other ion-exchanged samples,

resulting in a larger effective refractive index. Furthermore, the IE 4% sample shows lower disorder and smaller direct and indirect energy gap values, which causes a higher refractive index than the other samples.²⁹

As shown in Figure 5, the surface of the ion-exchanged glasses is not smooth due to the silver clusters on the surface. Therefore, the periodic nanostructures, which are formed on the ion-exchanged glasses, are not perfect nanogratings. To find out how well the silver nanogratings are formed on the surface of the samples, the optical density spectra of each sample are measured by a linearly polarized probe beam, in both parallel (\parallel) and perpendicular directions (\perp) to the nanograting. A more ordered silver nanograting would yield a more considerable difference between the two optical densities.

The optical density spectra of the silver nanograting formed on the soda-lime glass and IE 2%, IE 4%, and IE 6% samples by irradiating laser beam at a wavelength of 632.8 nm are indicated in Figure 8a-d, respectively.

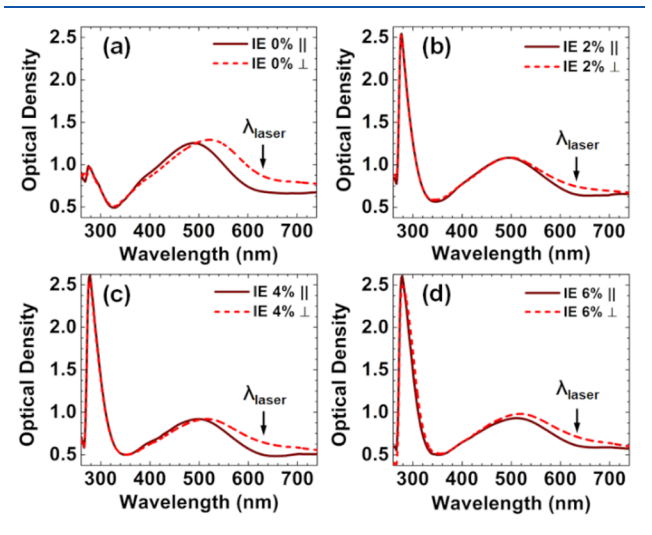


Figure 8. Polarized absorption spectroscopy for (a) soda-lime glass, (b) IE 2% sample, (c) IE 4% sample, and (d) IE 6% sample.

In Figure 8, the optical density spectra are measured by linearly polarized probe beams in two directions. At 632.8 nm, the absorption of the probe beam for which the polarization direction is perpendicular to the nanograting line (\bot) is larger for all samples. The difference of optical density spectra measured in two directions is maximum for soda-lime glass, as shown in Figure 8a. Since silver nanoparticles on the surface of the ion-exchanged samples increase the light scattering, the light propagation in IE samples is not as much intense as that in soda-lime glass. Therefore, the difference of the optical density spectra in two directions decreases in ion-exchanged samples compared to that in soda-lime glass. The difference of optical density for the IE 4% sample is larger than the other ion-exchange samples. Therefore, the nanograting on the surface of the IE 4% sample is more organized, as shown in Figure 8c. It seems that, in the IE 4% sample at a wavelength of 632.8 nm, a part of scattered light from silver nanoparticles is directed to propagate in waveguide.

The optical density spectra of ion-exchanged samples in Figure 8 have prominent absorption peaks in the vicinity of 300 nm, attributed to Ag⁺s, as mentioned before. Therefore, the low-power laser beam cannot neutralize Ag⁺s or induce any changes in the structure of the ion-exchange samples. The

absorption of the ion-exchanged samples covered by the Ag-AgCl layer is low at the laser wavelength. Therefore, the beam is coupled inside the ion-exchanged waveguide and propagates without considerable absorption. Ion-exchanged waveguides are long-term stable materials for optical applications. 42

CONCLUSIONS

Ion-exchanged glasses with three different ratios of Ag-NO₃:NaNO₃ salt (2:98, 4:96, and 6:94) were produced by a thermal process. The optical and structural analyses of the ionexchanged samples showed that, when silver ions saturate the surface of the ion-exchange glasses, e.g., in the IE 6% sample, no more silver ions and nanoparticles could penetrate into the glass matrix. Therefore, the formation of silver nanoclusters on the sample surface prevents further modification of the glass refractive index. The coupling of laser beam inside ionexchanged glasses was achieved readily by coating the Ag-AgCl layer on the glass surfaces. The formation of silver nanoparticle-based nanograting on the surface of ion-exchanged glasses couples the laser beam into the glass. Furthermore, the effective refractive index of the modified glass could be evaluated from the line-spacing of the silver nanograting. Therefore, the deposition of the Ag-AgCl layer on the ionexchange waveguide provides a platform that the laser beam could be coupled inside the waveguide and simultaneously provides a facile approach to determine the effective refractive index of the ion-exchanged waveguide. This paper supplies an original and novel way to couple light into the ion-exchanged waveguides for future applications such as optical communications and optical sensing.

ASSOCIATED CONTENT

Supporting Information

The Supporting Information is available free of charge at https://pubs.acs.org/doi/10.1021/acsanm.2c00438.

The ion-exchanged samples; the Lorentzian function fitted to the optical density spectra of ion-exchanged samples (IE 2%, IE 4%, and IE 6%); peak position and width of Lorentz curves; XRD patterns of IE 2%, IE 4%, and IE 6% samples; XPS broad spectra of soda-lime glass and ion-exchanged samples; the intensity, FWHM, and binding energy of Ag⁰ and Ag⁺ peaks; the O 1s core-level of soda-lime glass and ion-exchanged samples; the C 1s core-level of soda-lime glass and ion-exchanged samples; AFM images of the ion-exchanged sample surfaces; and FFT features of SEM images (PDF)

AUTHOR INFORMATION

Corresponding Author

Razieh Talebi — Department of Physics, University of Isfahan, 81747-73441 Isfahan, Iran; Quantum Optics Group, Department of Physics, University of Isfahan, 81747-73441 Isfahan, Iran; orcid.org/0000-0003-0209-2992; Email: r.talebi@sci.ui.ac.ir

Authors

Maedeh Aslani – Department of Physics, University of Isfahan, 81747-73441 Isfahan, Iran

Daryoosh Vashaee – Department of Electrical and Computer Engineering, North Carolina State University, Raleigh, North Carolina 27606, United States; Department of Materials Science and Engineering, North Carolina State University, Raleigh, North Carolina 27606, United States; occid.org/0000-0003-3667-3672

Complete contact information is available at: https://pubs.acs.org/10.1021/acsanm.2c00438

Author Contributions

R.T. conceived the idea and supervised the project. M.A. prepared the samples. D.V. performed the XPS and AFM experiments. R.T. and M.A. carried out the data analyses. The first draft was prepared by R.T. and edited and finalized by all authors.

Funding

D.V. received partial support from NSF under grant numbers ECCS-1711253 and CBET-2110603.

Notes

The authors declare no competing financial interest.

ACKNOWLEDGMENTS

R.T. acknowledges Prof. Hassan Sabzyan from the University of Isfahan for helpful discussions.

ABBREVIATIONS

IE, ion exchange Ag⁺s, silver ions Ag-AgCl, silver—silver chloride AgNO₃, silver nitrate NaNO₃, sodium nitrate SPR, surface plasmon resonance FWHM, full width at half-maximum NBO, non-bridging oxygens BO, bridging oxygens RID, refractive index dispersion

REFERENCES

- (1) Rahman, A.; Mariotto, G.; Cattaruzza, E.; Trave, E.; Gonella, F.; Quaranta, A. Thermal annealing and laser induced structural rearrangement and silver state modification in Ag⁺-Na⁺ ion-exchanged silicate glasses studied by Raman spectroscopy. *J. Non-Cryst. Solids* **2021**, 563, 120815.
- (2) Sheng, J.; Li, J.; Yu, J. The development of silver nanoclusters in ion-exchanged soda-lime silicate glasses. *Int. J. Hydrogen Energy* **2007**, 32, 2598–2601.
- (3) Rogozinski, R. Stresses produced in the BK7 glass by the K^+ Na^+ ion exchange: real-time process control method. *App. Sci.* **2019**, *9*, 2548.
- (4) Honkanen, S.; West, B.; Yliniemi, S.; Madasamy, P.; Morrell, M.; Auxier, J.; Schülzgen, A.; Peyghambarian, N.; Carriere, J.; Frantz, J.; Kostuk, R. Recent advances in ion exchanged glass waveguides and devices. *Phys. Chem. Glass* **2006**, *47*, 110–120.
- (5) Tervonen, A.; Honkanen, S.; West, B. Ion-exchanged glass waveguide technology: A review. Opt. Eng. 2011, 50, No. 071107.
- (6) Jose, G.; Sorbello, G.; Taccheo, S.; Valle, G. D.; Cianci, E.; Foglietti, V.; Laporta, P. Ag⁺–Na⁺ ion exchange from dilute melt: guidelines for planar waveguide fabrication on a commercial phosphate glass. *Opt. Mater.* **2003**, *23*, 559–567.
- (7) Kilislioglu, A. Ion exchange technologies; InTech, 2012, DOI: 10.5772/2925.
- (8) Nahal, A.; Jalehdoost, A.; Hassani, K.; Farokhniaee, A. Variation of index of refraction in the ion-exchanged glasses with the evolution of ionic and neutral silver nano-clusters. *Eur. Phys. J. Appl. Phys.* **2011**, 53, 10701.
- (9) Sonal; Sharma, A.; Aggarwal, S. Aggarwal, S. Optical investigation of soda lime glass with buried silver nanoparticles

- synthesised by ion implantation. J. Non-Cryst. Solids 2018, 485, 57–65.
- (10) Campbell, J. H.; Hayden, J. S.; Marker, A. High-power solid-state lasers from a laser glass perspective. *Int. J. Appl. Glass Sci.* **2010**, 2. 2.
- (11) Bloemer, M. J.; Haus, J. W. Broadband waveguide polarizers based on the anisotropic optical constants of nanocomposite films. *J. Light. Technol.* **1996**, *14*, 1534–1540.
- (12) Lopez-Lago, E.; Linares, J.; Salmio, R. P.; Saarinen, J.; Kuittinen, M.; Turunen, J.; Vahimaa, P. Modeling and interference-microscopy characterization of graded index transitions in ion exchange waveguide integrated elements: transitions between annealed surfaces. *Opt. Quantum Electron.* **2000**, *32*, 1269–1281.
- (13) Hunsperger, R. G. Integrated Optics; Springer, 2002.
- (14) Kufner, M.; Kufner, S. Ion exchange technology for optical waveguides. *Opt. Photonik* **2011**, *6*, 32–34.
- (15) Tellez-Limon, R.; Blaize, S.; Gardillou, F.; Coello, V.; Salas-Montiel, R. Excitation of surface plasmon polaritons in a gold nano slab on ion-exchanged waveguide technology. *Appl. Opt.* **2020**, *59*, 572–578.
- (16) Tellez-Limon, R.; Gardillou, F.; Coello, V.; Salas-Montiel, R. Coupled localized surface plasmon resonances in periodic arrays of gold nanowires on ion-exchange waveguide technology. *J. Opt.* **2021**, 23, 25801.
- (17) Righini, G. C.; Liñares, J. Active and Quantum Integrated Photonic Elements by Ion Exchange in Glass. *Appl. Sci.* **2021**, *11*, 5222.
- (18) Broquin, J.-E.; Honkanen, S. Integrated Photonics on Glass: A Review of the Ion-Exchange Technology Achievements. *Appl. Sci.* **2021**, *11*, 4472.
- (19) Ahmed, A. A.; Abd-Allah, E. W. Origin of Absorption Bands Observed in the Spectra of Silver ion-exchanged Soda–Lime–Silica Glass. *J. Am. Ceram. Soc.* **1995**, *78*, 2777.
- (20) Madrigal, J. B.; Tellez-Limon, R.; Gardillou, F.; Barbier, D.; Geng, W.; Couteau, C.; Salas-Montiel, R.; Blaize, S. Hybrid integrated optical waveguides in glass for enhanced visible photoluminescence of nanoemitters. *Appl. Opt.* **2016**, *55*, 10263.
- (21) Yulianto, M.; Marzuki, A.; Suryanti, V. 2017 Fabrication and characterization planar waveguides of Na+-Ag+/K+ by ion exchange and prism coupler; AIP Conference Proceedings, 1868, 060006.
- (22) Berneschi, S.; Righini, G. C.; Pelli, S. Towards a glass new world: The role of ion-exchange in modern technology. *Appl. Sci.* **2021**, *11*, 4610.
- (23) Ageev, L. A.; Miloslavsky, K. Photoinduced effects in light-sensitive films. *Opt. Eng.* **1995**, *34*, 4.
- (24) Talebi, R.; Izadi, S. Investigating surface morphology of Ag-AgCl thin film by scattering pattern at normal and oblique incident angles. *Appl. Opt.* **2018**, *57*, 10355–10363.
- (25) Talebi, R.; Taheri Ghahfarokhi, F.; Vashaee, D. Photoinduced tunable birefringence and dichroism in silver nanogratings. *J. Opt. Soc. Am. B* **2020**, *37*, 2848–2855.
- (26) Berg, K.-J.; Berger, A.; Hofmeister, H. Small silver particles in glass surface layers produced by sodium-silver ion exchange-their concentration and size depth profile. *Z. Phys. D* **1991**, *20*, 309–311.
- (27) Varma, R. S.; Kothari, D. C.; Tewari, R. Nano-composite soda lime silicate glass prepared using silver ion exchange. *J. Non. Cryst. Solid* **2009**, 355, 1246.
- (28) Mohr, C.; Dubiel, M.; Hofmeister, H. J. Phys.: Condens. Matter 2001, 13, 525.
- (29) Kchaou, H.; Karoui, K.; Khirouni, K.; Ben Rhaiem, A. Optical and dielectric relaxation of transition metal-based organic-inorganic hybrid materials. *J. Alloys Compd.* **2017**, 728, 936–943.
- (30) Yanıka, M. C. Ö.; Sarıgüzela, M.; Öztürka, Y.; Yıldızb, T.; Kaçarb, E. D.; İyielb, A.; İzmirlioğlub, B.; Günaya, E. Influence of different process conditions on mechanical, optical and surface properties of silver ion exchanged soda-lime silicate glass. *J. Non. Cryst. Solid* **2018**, 493, 1.
- (31) Rajith Kumar, C. R.; Betageri, V. S.; Nagaraju, G.; Pujar, G. H.; Suma, B. P.; Latha, M. S. Photocatalytic, nitrite sensing and

antibacterial studies of facile bio-synthesized nickel oxide nanoparticles. J. Sci.: Adv. Mater. Devices 2020, 5, 48-55.

- (32) Mott, N. F.; Davis, E. A. Electronic Processes in Non-Crystalline Materials; Oxford, 1971.
- (33) Varma, R. S.; Kothari, D. C.; Mallik, A. K.; Bhatnagar, A.; Kanjilal, D.; Santra, S.; Thomas, R. G.; Tewari, R.; Neogy, S.; Dey, G. K. Optical properties of ion exchanged and swift heavy ion beam treated silicate glasses. Adv. Mater. Lett. 2015, 6, 425.
- (34) Anyaegbunam, F. N. C.; Augustine, C. A study of optical band gap and associated Urbach energy tail of chemically deposited metal oxide binary thin film. Dig. J. Nanomater. Biostructures 2018, 13, 847.
- (35) Dhoondia, Z. H.; Chakraborty, H. Lactobacillus mediated synthesis of silver oxide nanoparticles. Nanomater. Nanotechnol. 2020, 2, 15.
- (36) Inácio, P. L.; Barreto, B. J.; Horowitz, F.; Correia, R. B.; Pereira, M. B. Silver migration at the surface of ion-exchange waveguides: a plasmonic template. Opt. Mater. Express 2013, 3, 390-399.
- (37) Mathpal, M. C.; Kumar, P.; Kumar, S.; Tripathi, A. K.; Singh, M. K.; Prakash, J.; Agarwal, A. Opacity and plasmonic properties of Ag embedded glass based metamaterials. RSC Adv. 2015, 5, 12555.
- (38) Cheng, W.; Wu, Z.; Gu, X.; Xing, X.; Mo, G.; Wu, Z. Grazing incidence small angle X-ray scattering study of silver nanoparticles in ion-exchanged glasses. Nucl. Instrum. Methods Phys. Res. B 2015, 351,
- (39) Calderon, V. S.; Galindo, E.; Benito, N.; Palacio, C.; Cavaleiro, A.; Carvalho, S. Ag⁺ release inhibition from ZrCN-Ag coatings by surface agglomeration mechanism: structural characterization. J. Phys. D: Appl. Phys. 2013, 46, 325303.
- (40) Gongalsky, M. B.; Kargina, J. V.; Cruz, J. F.; Sánchez-Royo, J. F.; Chirvony, V. S.; Osminkina, L. A.; Sailor, M. J. Formation of Si/ SiO₂ luminescent quantum dots from mesoporous silicon by sodium tetraborate/citric acid oxidation treatment. Front. Chem. 2019, 7, 165.
- (41) Kolobkova, E.; Kuznetsova, M. S.; Nikonorov, N. Ag/Na ion exchange in fluorophosphate glasses and formation of Ag nanoparticles in the bulk and on the surface of glass. ACS Appl. Nano Matter. 2019, 2, 6928-6938.
- (42) Simo, A.; Joseph, V.; Fenger, R.; Kneipp, J.; Rademann, K. Long-Term Stable Silver Subsurface Ion-Exchanged Glasses for SERS Applications. ChemPhysChem 2011, 12, 1683-1688.

□ Recommended by ACS

Femtosecond-Laser-Induced Saturable Absorption and **Optical Limiting of Hollow Silver Nanocubes: Implications** for Optical Switching and Bioimaging

Bhavesh K. Dadhich, Amiya Priyam, et al.

NOVEMBER 05, 2020

ACS APPLIED NANO MATERIALS

RFAD

Nanoscale-Thick Silver Black Films Fabricated in He/Ar **Inert Gas Conditions for Broadband Absorbers**

Yan Hao, Yongming Zhao, et al.

JUNE 06, 2022

ACS APPLIED NANO MATERIALS

READ M

Ag-Diamond Core-Shell Nanostructures Incorporated with **Silicon-Vacancy Centers**

Shuo Li, Robert J. Hamers, et al.

OCTOBER 22, 2021

ACS MATERIALS AU

READ [7

Enhancement of Raman Scattering and Exciton/Trion Photoluminescence of Monolayer and Few-Layer MoS2 by Ag Nanoprisms and Nanoparticles: Shape and Size Effects

Iqra Irfan, Junle Qu, et al.

FEBRUARY 15, 2021

THE JOURNAL OF PHYSICAL CHEMISTRY C

RFAD

Get More Suggestions >